Developing aerodynamic design diagnostics for control of interior wind noise

P. Bremner

AeroHydroPLUS, 2311 Via Aprilia, Del Mar, 92014, USA

pbremner@aerohydroplus.com

The author will discuss various ways that we can use our understanding of how wall pressure fluctuations generate interior noise, to provide aerodynamic design guidance for control of wind noise. New quantitative diagnostics discussed will include visualization of k-filtered acoustic loading in turbulence, calculation of flow-induced dipole sources of acoustic loading and direct measurement of acoustic loading under turbulence, which can be applied to clay models in the wind tunnel.

1 Introduction

Full simulation of wind noise transmission is feasible today, using time-accurate computational fluid dynamics (CFD) to provide nodal pressure loading to a numerical vibro-acoustics model. However, even when this modeling approach is fully validated, on its own it provides very little guidance to aerodynamic shape design for attenuation or refinement of transmitted wind noise. There is a need to develop intermediate diagnostics from the numerical model results, as well as complementary diagnostics that can be implemented during aeroacoustic wind tunnel testing. This paper describes four diagnostics that are being developed to guide aeroacoustic design, with application to wind noise from an automotive side glass with a mirror protuberance.

Section 2 reviews source and transmission path component diagnostics that can be adopted from statistical energy analysis (SEA). Section 3 introduces a method to visualize the important low wave number source characteristics in typical CFD results. Section 4 describes a boundary element modeling method to quantify the components of exterior acoustic loading from turbulence–generated dipole sources. Section 5 demonstrates the use of a simple stick-on/peel-off microphone array to generate wavenumber-frequency spectrum diagnostics directly from wind tunnel testing of clay models and prototype vehicles.

2. Acoustic Power Transmission

We are concerned here with the aero-vibro-acoustics problem of the transmission of unsteady exterior aerodynamic surface pressure fluctuations through a flexible (vibrating) structure, and the resulting sound power radiated to the interior of an enclosed vehicle.
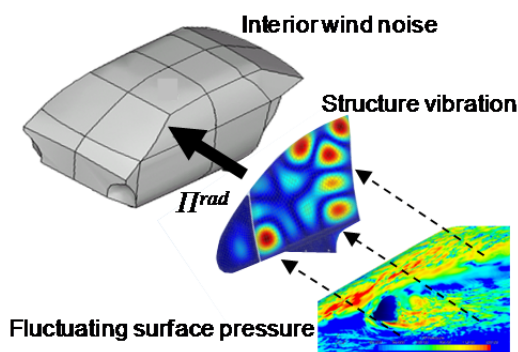
Figure 1 Elements of a wind noise transmission model[1]

It has been shown [1] shown that for quite general unsteady aerodynamic loading, the sound power spectral density transmitted by a vibrating structure is

$$\Pi^{rad}(\omega) \propto \rho_0 c_0 A \sum_r \frac{\omega^2 S_{ff,r}(\omega)\sigma_r(\omega)}{\mu_r^2 |Y_r(\omega)|^2} \qquad (1)$$

where $Y_r(\omega) = [\omega_r^2 + i\eta_r\omega\omega_r - \omega^2]$ is the structure modal receptance and μ_r is the modal mass. The modal force spectral density $S_{ff,r}$ is a double area integral of surface pressure cross spectral density $G_p(\underline{x}, \underline{x}'; \omega)$ and $\psi_r(\underline{x})$, the rth panel mode shape,

$$S_{ff,r}(\omega) = \iint_A \psi_r(\underline{x}) G_p(\underline{x}, \underline{x}'; \omega) \psi_r(\underline{x}') \, d\underline{x} d\underline{x}' \qquad (2)$$

This can be computed explicitly from the nodal pressure time histories provided by time accurate CFD, where computational effort is usually minimized by modal reduction of the pressure time histories before computing the cross spectrum matrix, or by truncated proper orthogonal decomposition of pressure time histories, or both. A third reduction is to calculate the wavenumber-frequency spectrum of the pressure time histories $\Phi_p(\underline{k}, \omega)$ and the wavenumber spectrum of the structure modes shapes [6], in which case the modal force spectral density simplifies to a single area integral

$$S_{ff,r}(\omega) = \int \Phi_p(\underline{k}, \omega) |\psi_r(\underline{k})|^2 \, d\underline{k} \qquad (3)$$

The fourth term in (1) is the modal radiation efficiency [2]

$$\sigma_r(\omega) = \frac{k_0^2}{2\pi A} \iint_A \psi_r(\underline{x}) \frac{\sin[k_0(\underline{x} - \underline{x}')]}{k_0(\underline{x} - \underline{x}')} \psi_r(\underline{x}') \, d\underline{x} d\underline{x}' \qquad (4)$$

where $k_0 = \omega/c_0$ is the acoustic wavenumber. This can be computed numerically, directly from finite element representation of nodal vibration responses, using any of the efficient Rayleigh integral schemes [3] or equivalent direct integration of sound intensities from a boundary integral equation solution. A third reduction is a single area integral in the wavenumber domain [6]

$$\sigma_r(\omega) = \frac{k_0^2 A}{2\pi} \int_{|k_r| < k_0} \left[1 - \left(\frac{k_r^2}{k_0^2}\right)\right]^{-0.5} |\psi_r(\underline{k})|^2 \, d\underline{k} \qquad (5)$$

where $k_r^2 = k_x^2 + k_y^2$ and wavenumber transform of the rth mode shape is $\psi_r(k) = 1/\sqrt{2\pi} \int \psi_r(\underline{x}) e^{-ikx} d\underline{x}$

2.1. Modal Contribution Diagnostics

A first level diagnostic is to consider the sound power transmission by each mode. Since there can be a large number of structural modes in the audible frequency range [typically O^2-O^4], a more practical diagnostic is to compute the sound power transmitted in any frequency band $\Delta\omega$ in

three modal partitions – i) resonant modes $\omega_r \in \Delta\omega$, ii) mass-controlled modes $\omega_r < \Delta\omega$ and iii) stiffness-controlled modes $\omega_r > \Delta\omega$. Stiffness-controlled modes will only contribute for highly localized loading – such as direct field radiation under a point force [4] - and are commonly neglected. The wind noise sound power transmitted in frequency band $\Delta\omega$ can then be quantified as contributions from resonant modes (which can be attenuated by mass and damping of the structure) and non-resonant, mass-controlled modes (which can only be attenuated by mass)

$$\Pi_{\Delta\omega}^{rad} \propto \rho_0 c_0 A \int_{\Delta\omega} d\omega \left\{ \sum_{r:\,\omega_r \in \Delta\omega} \frac{\omega^2 S_{ff,r}(\omega)\sigma_r(\omega)}{m_r^2 \left| Y_r(\omega) \right|^2} \right.$$
$$\left. + \sum_{r:\,\omega_r < \Delta\omega} \frac{S_{ff,r}(\omega)\sigma_r(\omega)}{\omega^2 m_r^2} \right\} \qquad (6)$$

2.2.   Acoustics versus Turbulence Loading Contribution Diagnostics

For low subsonic flow speeds, it has been shown [5],[6] that fluctuating surface pressure (FSP) loading will be strongly filtered by the vehicle structural and acoustic wavenumbers. At these low wavenumbers, there are two distinct aeroacoustic processes operating – convecting turbulence and acoustic wave propagation. Bremner and Wilby [6] have suggested that the FSP frequency-wavenumber spectrum can be separated into two components

$$\Phi_p(k,\omega) = \Phi_c(k,\omega) + \Phi_0(k,\omega) \qquad (7)$$

where Φ_c is the convecting turbulence component and Φ_0 is the acoustic component generated by, or propagating within, the turbulence.
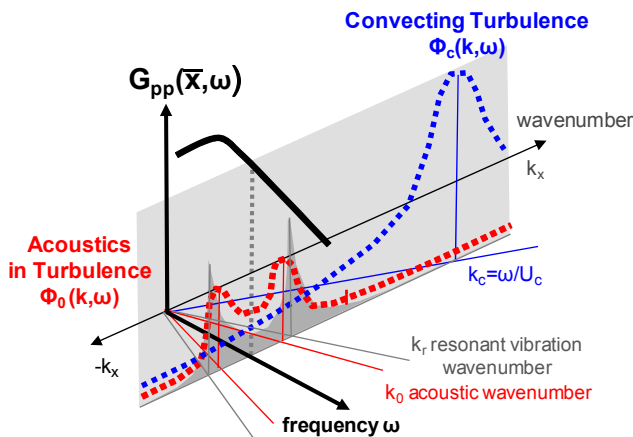
Figure 2 Streamwise wavenumber decomposition of a typical boundary layer surface pressure spectrum, showing both turbulence (blue) and acoustic components (red) at low wavenumber, with wavenumber content of a coincident structural resonance (grey) superimposed

While this separation of loading is necessary for a statistical energy analysis (SEA) solution of (1), it is also an important contribution diagnostic which should be considered in any wind noise transmission analysis.

Combining (6) and (7) yields four useful diagnostic components – resonant mode transmission of low wavenumber turbulence and separately, acoustics in turbulence; and non-resonant (mass-controlled) transmission of the low wavenumber turbulence and acoustic loading components:

$$\Pi_{\Delta\omega}^{rad} \propto \rho_0 c_0 A \int_{\Delta\omega} d\omega \left\{ \sum_{r:\,\omega_r \in \Delta\omega} \frac{\omega^2 \left[S_{ff,r}^c(\omega) + S_{ff,r}^0(\omega) \right] \sigma_r}{\mu_r^2 \left| Y_r(\omega) \right|^2} \right.$$
$$\left. + \sum_{r:\,\omega_r < \Delta\omega} \frac{\left[S_{ff,r}^c(\omega) + S_{ff,r}^0(\omega) \right] \sigma_r}{\omega^2 \mu_r^2} \right\} \qquad (8)$$

where $\quad S_{ff,r}^c(\omega) = \int \Phi_c(\underline{k},\omega) \left| \psi_r(\underline{k}) \right|^2 d\underline{k} \qquad (9)$

and $\quad S_{ff,r}^0(\omega) = \int \Phi_0(\underline{k},\omega) \left| \psi_r(\underline{k}) \right|^2 d\underline{k} \qquad (10)$

2.3.   Idealized Side Mirror Case

The fluctuating pressure loading on the surface of a flat panel with an idealized mirror protuberance was obtained in Figure **3** from time-accurate, compressible hybrid RANS-LES simulation using STAR-CCM+ [8],[9].
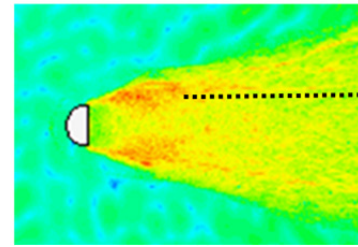
Figure 3 Fluctuating surface pressure behind side mirror

The wavenumber-frequency spectrum of FSP is shown in Figure **4**. The dominant pressure fluctuations are concentrated at the turbulence convection wavenumber $k_c = 2\pi f/U_c$. However, in the low wavenumber region, it is clear that loading in the acoustic wavenumber range $k = \pm 2\pi f/c_0$ can be substantially higher that turbulence loading.
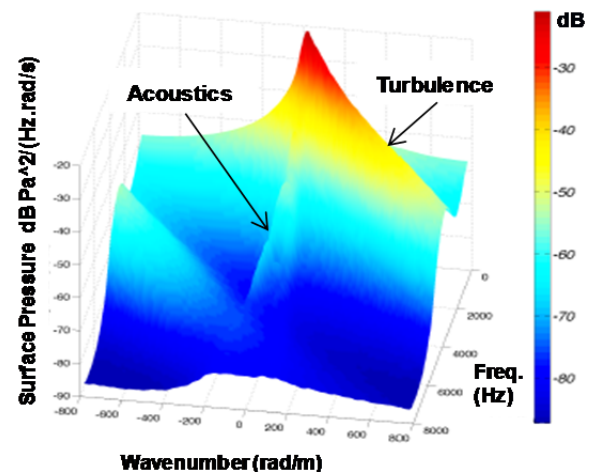
Figure 4 Wavenumber-frequency spectrum of fluctuating surface pressure from streamwise array in Figure 3

2.4.   SAE Body Case

For the SAE body study [7] (and Figure 6), the acoustic loading was obtained by wavenumber analysis for the more complex 3-dimensional flow over the side glass region of vehicle body shape. The total acoustic energy was found to be equal to the convecting turbulence energy at 4,000Hz, but substantially less at lower frequencies, as shown in Figure 5.
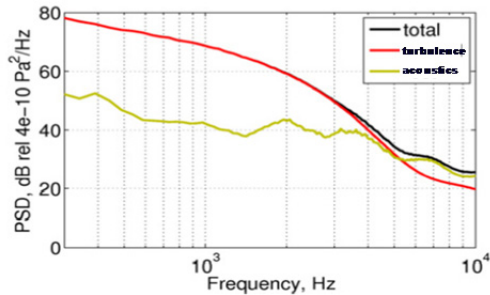
Figure 5 Fluctuating surface pressure level on the SAE body side glass with mirror, showing acoustic loading and turbulence loading components (from [7])

The present author has used the SEA model shown in Figure 6 to demonstrate the diagnostics described in 2.2.
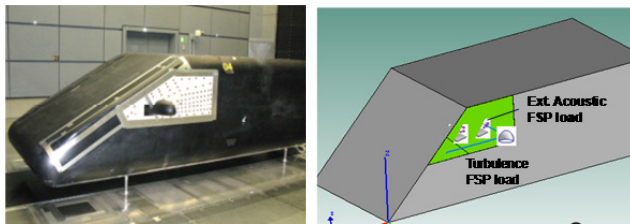
Figure 6 The SAE body (left) and SEA model of side glass wind noise transmission (right), with separate turbulence and exterior acoustic FSP loading

Predicted side glass vibration is shown in Figure 7. It can be seen that the turbulence loading matches measured vibration at low frequencies 400 – 1,250 Hz. Above 1,250 Hz, the exterior acoustic loading controls the glass vibration.
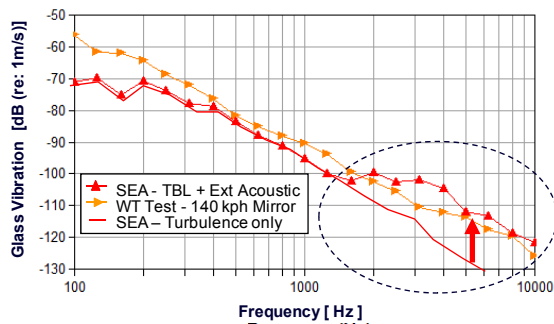
Figure 7 SEA predicted side glass vibration compared to measured vibration in 1/3 octaves; for turbulence loading and for combined turbulence and acoustics loading

Predicted interior sound pressure level (SPL) is shown in Figure 8. It can be seen that the turbulence loading is responsible for most of the sound transmission at low frequencies. Acoustic loading contributes an additional 3dB

in the frequency range 200 – 1,250 Hz.   Above 1,250 Hz, the exterior acoustic loading controls the interior SPL.
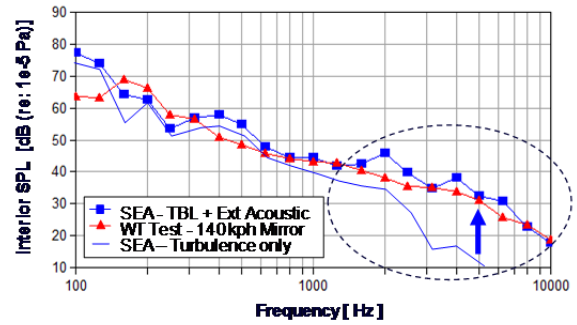
Figure 8 SEA predicted interior SPL compared to measured SPL in 1/3 octaves; for turbulence loading and for combined turbulence and acoustics loading

By computing the diagnostic components of wind noise sound transmission, as defined in 2.1 and 2.2, the relative contributions can be quantified to guide vibro-acoustic design. The sound power contributions result in Figure 9 shows that for the SAE body, side glass wind noise below 1,250 Hz may have approximately equal contributions from *resonant* glass response to turbulence and *non-resonant* (mass-controlled) transmission of exterior acoustics.
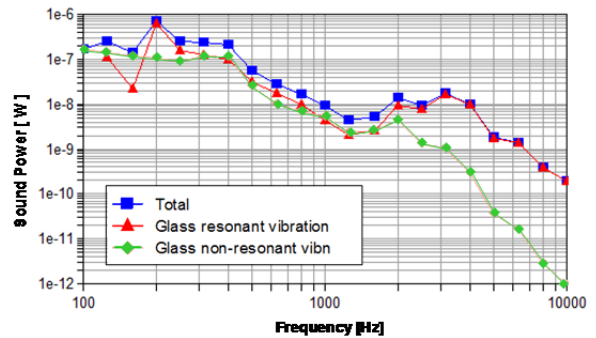
Figure 9 Sound power contributions to interior SPL

3. Visualizing Aero-acoustic Sources

To guide aerodynamic shape design for wind noise, it is natural to look at the spectrum and spatial distribution of the fluctuating surface pressures (FSP). As part of the SAE body study [7], the authors used an array of surface mounted microphones (shown in Figure 6) to measure changes in FSP for three different mirror configurations – baseline mirror, enlarged mirror and no mirror. The space-averaged FSP result is shown in Figure 10.
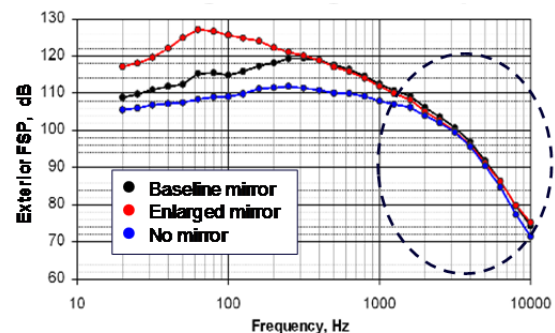
Figure 10 Space-averaged, side glass FSP for SAE body with 3 mirror configurations at 0° yaw, 140 km/h (from [7])

The corresponding change in interior sound pressure level (SPL) is shown in Figure 11.
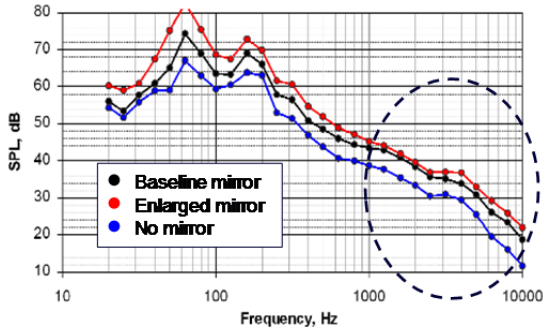
Figure 11 Interior SPL for SAE body with three mirror configurations at 0° yaw, 140 km/h (from [7])

It is confounding (but common) to observe that while the interior SPL changes by 3-6dB with each mirror change, the space-averaged exterior FSP loading shows little or no change in the sensitive audible frequency range 1-10kHz.   It is evident that subtle changes in aerodynamic design can have a significant impact on the low wavenumber and/or exterior acoustic loading, *without* a proportional change in the convecting turbulence FSP loading.

Using CFD to try to visualize the impact of aerodynamic design changes on the important underlying low wavenumber loading can be equally unrewarding. This is simply because the larger amplitude convection wavenumber turbulence FSP levels obscure the low wavenumber and acoustic wavenumber components of the flow. For the idealized side mirror case, the cross spectrum phase plot in Figure 12 shows that an acoustic field *is* present in the compressible LES solution [10], but only visible as long wavelength propagation *outside* the hydrodynamic turbulence wake.   The low wavenumber acoustic loading under the wake is obscured.
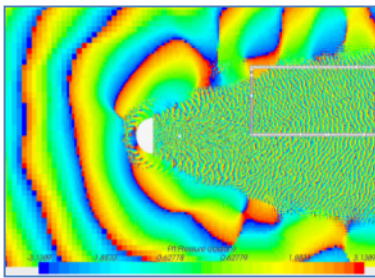
Figure 12 Cross spectrum phase plot at 2,000 Hz, for the fluctuating surface pressure around an idealized side mirror (from [10])

3.1. Visualizing Low Wavenumber Loading

With the aim of visualizing the low wavenumber and acoustic loading "buried" in the side glass turbulence, this study exploited the ability to reconstruct the spatial pressure time history from a complex (single block) pressure wavenumber-frequency (k-f) spectrum by inverse Fourier transform (IFT):

$$p\left(\underline{x},t\right) = \frac{1}{\left(2\pi\right)^{3}} \iiint e^{-i\omega t} e^{ik\,\underline{x}} \Phi\left(\underline{k},\omega\right) d\underline{k}\,d\omega \qquad (11)$$

The "acoustic" component of spatial pressure time history $p_0\left(\underline{x},t\right)$ can be wavenumber filtered and frequency band filtered within the inverse Fourier transform:

$$p_{0,\Delta\omega}\left(\underline{x},t\right) = \frac{1}{\left(2\pi\right)^{3}} \iiint e^{-i\omega t} e^{ik\,\underline{x}} W_{\Delta\omega}\left(\omega\right) W_0\left(\underline{k}\right) \Phi\left(\underline{k},\omega\right) d\underline{k}\,d\omega$$

$$(12)$$

The wavenumber filter function $W_0\left(k_x, k_y\right)$ and frequency filter function $W_{\Delta\omega}\left(\omega\right)$ are shown in Figure 13 below:
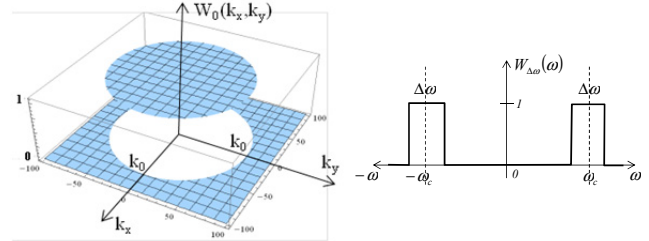
Figure 13 The spatial wavenumber filter function (left) and temporal frequency filter function (right)

An instantaneous snap shot of the re-constructed acoustic field for a frequency band centered on 1,000 Hz is shown in Figure 14 for the idealized side mirror wake. The plot on the left is the total fluctuating pressure with characteristically short wavelength pressure fluctuations of the convecting turbulence. The plot on the right shows the much longer wavelength, but lower level acoustic loading.
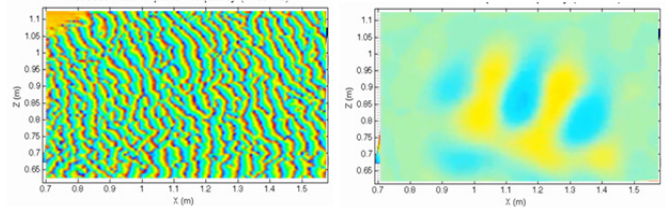
Figure 14 Fluctuating surface pressure snap shot in a frequency band centered at 4,000 Hz; total pressure (left) and underlying k-filtered acoustic pressure (right)

The author is now using 3D acoustic field animations such as those in Figure 15, to guide aerodynamics shape design.
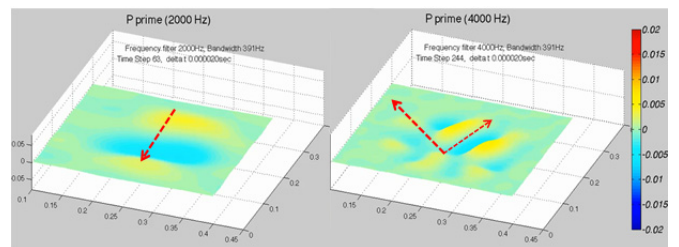
Figure 15 Snap shots of 3D animations of side glass acoustic loading for frequency bands centered at 2,000 Hz (left) and 4,000 Hz (right)

Animation of the full surface, k-filtered acoustic pressure time history typically shows propagation downstream from the dominant side mirror acoustic source, with smaller uncorrelated acoustic waves mixing from other directions. The latter are associated with propagation from

other (weaker) acoustic sources, such as the A-pillar and B-pillar, and can be separated using directional wavenumber filtering or using principal component analysis.

4. Quantifying Exterior Acoustic Sources

Visualizing the low wavenumber and acoustic loading in a turbulent exterior flow field is one step towards facilitating quantitative aerodynamic shape design for wind noise reduction. The other essential step is to try to relate specific aerodynamic styling features to component aero-acoustic sources strengths. This process is still in its infancy.

From Lighthill [11] we can expect acoustics to be generated by quadrapole sources in the turbulent flow over the vehicle. Far field acoustic beam forming – such as the results shown in Figure 16 – suggest that the strongest quadrapole noise is in the wake of the mirror. Quantifying this source directly from LES simulation is a challenging three dimensional volume integral, with the influence of significant acoustic scattering. Results reported by several recent studies are still being reviewed.
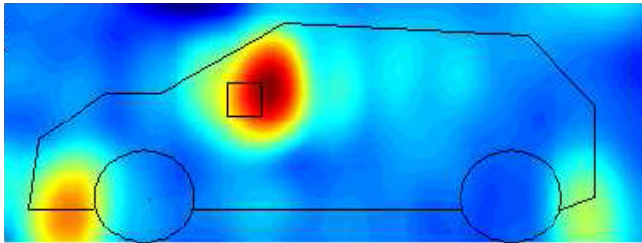
Figure 16 3-D beam forming of sound radiation from the side mirror of a vehicle at 1,600Hz, using CIRAS algorithm (from Picard [12])

From the work of Curle [13], we also expect dipole sources to arise from the incompressible turbulence pressure loading on surfaces. The strongest such sources are likely to be the side mirror, the A-pillar and the B-pillar. Since these source regions are on the boundary of the vibrating (sound transmission) surface, the corresponding acoustic loading on the glass is expected to be propagating across the surface, at approximately grazing incidence. Each of these source regions are separated by distances much greater than the correlation length of the hydrodynamic turbulence, so each will make a statistically uncorrelated contribution to the combined acoustic loading

4.1. Surface Dipole Contributions to Acoustics

Quantifying the acoustic source strength of turbulence interaction with surfaces is possible from an incompressible LES simulation, using an acoustics code.

For the idealized side mirror case, the fluctuating surface pressure (FSP) loads on the mirror surface - from an incompressible LES solution – were applied as a blocked pressure constraint to a boundary element acoustics model in the VA One software from ESI Group. Typical FSP loading at 500 Hz is shown in Figure 17 (top). The mirror hydrodynamic loading defines a complex surface dipole source distribution in the boundary element (BEM) acoustic

solution. The model includes a rigid scattering surface for the test panel on which the resulting acoustic loading at 500 Hz is predicted, as shown in Figure 17 (bottom).   A preliminary BEM solution was obtained over the frequency range 500 – 1,250 Hz.
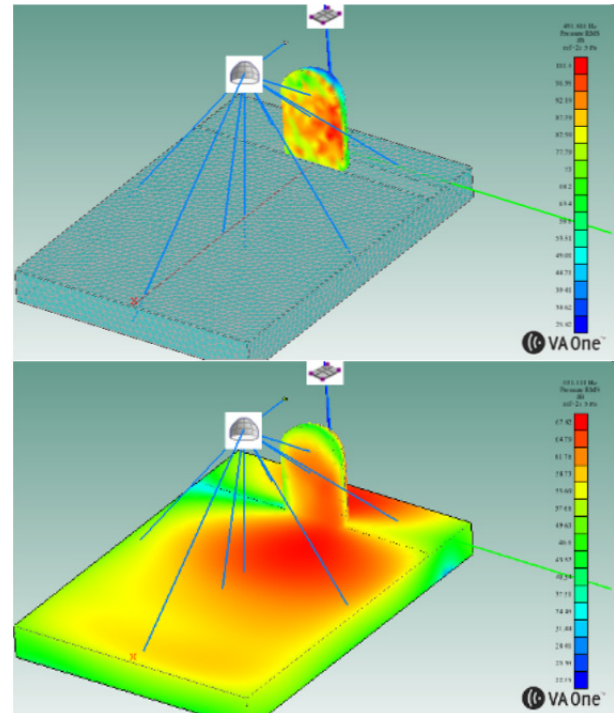
Figure 17 Acoustic model of dipole source radiation from mirror at 500 Hz; LES pressure loading on mirror (top) and mirror-radiated acoustic load on panel (bottom).

Since the acoustic source is localized at the mirror and there are no other reflective surfaces, the acoustic field on the panel surface propagates uni-directionally away from the mirror. The model estimate of the propagating acoustic loading spectrum is shown in Figure 18, compared with the total FSP spectrum and compared with the total acoustic wavenumber spectrum from the *compressible* LES loading on the panel.
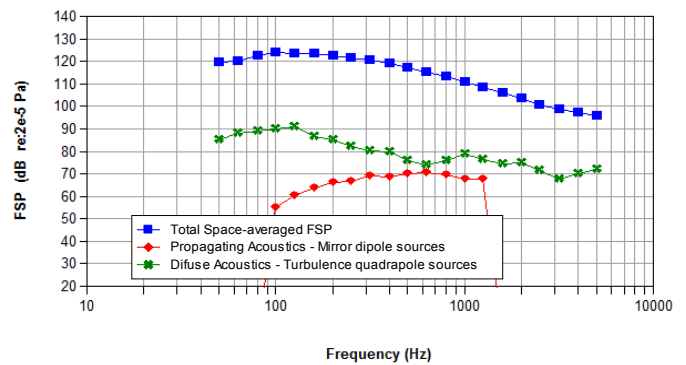
Figure 18 Fluctuating surface pressure for three components of aeroacoustic loading; total FSP (blue squares), total acoustic wavenumber loading (green crosses) and mirror dipole source (red diamonds).

For the idealized mirror geometry, the surface dipole acoustics source is predicted to be a contributor to the total acoustic wavenumber loading, which is responsible for wind noise transmission. This suggests a useful new

diagnostic to aerodynamic shape design for wind noise, and will be the subject of further research and evaluation.

5. Measurement of Acoustics in Turbulence

The ability to directly measure the low wavenumber aeroacoustic loading responsible for interior wind noise is another essential diagnostic, required for aerodynamic shape design. Such a capability is required for validation of LES simulations. However, a direct measurement of the low wavenumber source strength can also be used in an SEA model to predict interior wind noise, as shown in 2.4 (for the SAE body case). For a new vehicle program, measuring low wavenumber loading on a clay model in an aeroacoustic wind tunnel to directly evaluate interior wind noise sensitivity to aerodynamic design changes (eg different mirrors) may be faster or more cost effective than multiple time accurate, compressible CFD simulations.

Arguillat [14] has successfully measured the acoustic loading in turbulence using a line array of microphone "taps" to ¼ inch microphones. Gabriel [15] has used a novel 2-dimensional sparse array of very small digital MEMS microphones to measure the acoustic loading in turbulence. A typical example of a commercially available MEMS microphone widely used in mobile phones is shown in Figure 19. The main limitation of each of the foregoing arrays is that their installation is intrusive to the measurement surface.
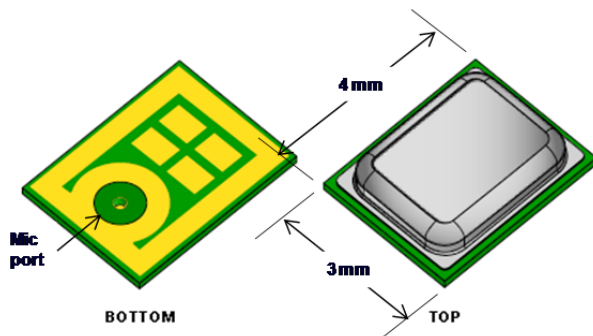
Figure 19 Commercial MEMS microphone dimensions

The author has contributed to the development of a non-intrusive "stick-on / peel-off" array configuration, which also reduces all wiring to a single USB connection, using a direct-data-to-memory configuration [16]. The essential performance requirements for the array are:

i. The microphones and data recording electronics must each have a signal-to–noise ratio of at least 65dB

ii. The array of microphones must be closely spaced at less than 3.5 mm centers, to ensure that the convecting turbulence FSP is not "aliased" into the wavenumber range of acoustics up to 5,000 Hz at 140 km/h

iii. The sensor array and all immediately adjacent data recording electronics and wiring must be very low aerodynamic profile and present a smooth surface to the flow to avoid instrumentation-induced perturbation to the boundary layer turbulence

iv. The sensor array and data recording electronics must be flexible enough to conform to the radius of curvature of the automotive body panel, to avoid local perturbation to the boundary layer turbulence

A prototype array has been designed, built and is currently being tested against these requirements. The prototype array uses thirty-two (32) MEMS digital microphones shown in Figure 20 (top).
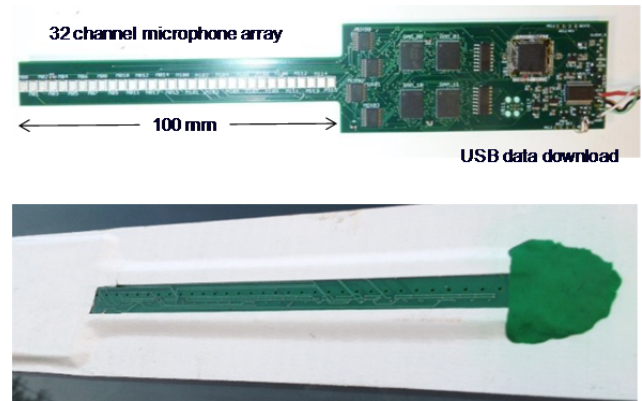
Figure 20 32 channel MEMS array, direct-wired to digital memory on a flexible PCB (top), showing microphone ports exposed on measurement surface (bottom)

The MEMS sensors are mounted on a flexible PCB substrate at uniform 3.5mm centers to form a simple line array. The holes in the other side of the PCB (Figure 20, bottom) are the pressure measurement ports. The high speed RAM and data clocking components are close-mounted to the end of the sensor array. All data traces from sensors to RAM chips are incorporated on the multi layer PCB. The combined thickness of MEMS microphones, memory chips and PCB can be kept as low as 2 mm, satisfying requirement iii. above. The design also tolerates static flexure on the flexible PCB when it is taped to the doubly-curved glass surface, thus satisfying the conformal array requirement iv. above.

FSP array data was acquired on the road at 80 mph with the array taped to the lower rear corner of the passenger side glass of a test automobile, as shown in Figure 21 (left).

Figure 21 Stick-on/peel-off design of the array - applied to an automobile side glass (left) and showing *in principle* application to clay model in wind tunnel (right)

The 32 digital outputs were recorded directly in RAM for a 3 second sample period and subsequently downloaded to a host PC using the USB port. The MEMS digital outputs were then converted to digital pressure time histories and Fourier transformed in time and space to generate the FSP wavenumber-frequency spectrum shown in Figure 22.

The high amplitude "ridge" at higher wavenumber is the expected convecting turbulence component of FSP. The lower amplitude ridge at lower wavenumbers centered around k=0 is the acoustic component of FSP.

These results show that the direct-data-to-memory array using MEMS microphones can meet the requirements of a

new diagnostic tool that would directly quantify acoustic loading in turbulence, for interior wind noise design
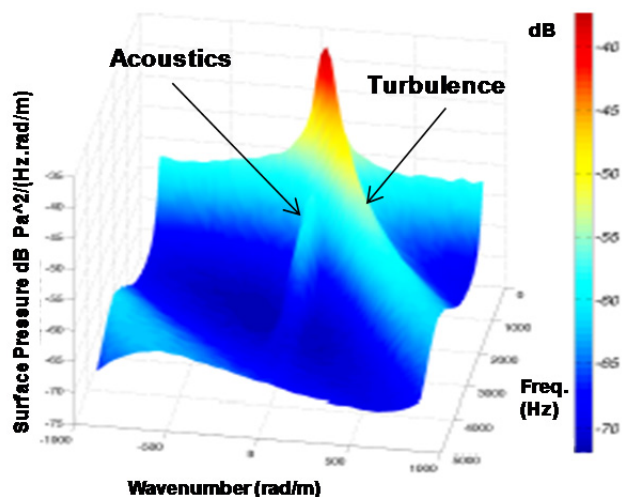
Figure 22 Wavenumber frequency spectrum of fluctuating pressure on side glass, clearly showing the separation of convecting turbulence and acoustic components.

6. Conclusion

New diagnostic methods have been defined and demonstrated, to enable a more quantitative approach to aerodynamic shape design for interior wind noise control and refinement.

The most fundamental diagnostic is the separation of resonant and non-resonant modal contributions; and separation of turbulence versus acoustic contributions. These diagnostics are recommended, regardless of whether one is using time-accurate, compressible CFD as direct nodal loading for a finite element model or a space-averaged reduction of the loading for an SEA vibro-acoustic model. This paper has described three additional diagnostics being developed to aid quantitative aerodynamic shape design for wind noise control. The three diagnostics are i) visualization of *k*-filtered acoustic wavenumber loading in turbulence, ii) calculation of flow-induced dipole sources of acoustic loading and iii) direct measurement of acoustic loading under turbulence, which can be applied to clay models in the wind tunnel.

References

[1] Bremner, P.G. "Finite Element based Vibro-Acoustics of Panel Systems", *Proc. 5th Intnl. Conf. on Finite Element Methods in Engineering*, Melbourne Australia, August 1987

[2] Leppington, F., Broadbent, E. and Heron, K. "The Acoustical Radiation Efficiency of Rectangular Panels" *Proc. R. Soc. Lond.* A 382, 1982

[3] Langley, R. "Numerical evaluation of the acoustic radiation from planar structures with general baffle conditions using wavelets" *J. Acoust. Soc. Am*. 121 (2), February 2007

[4] Fahy, F. "Sound and Structural Vibration", *Academic Press,* 1985

[5] Hwang, Y. and Maidanik, G. "A Wavenumber Analysis of the Coupling of a Structural Mode and Flow Turbulence" *Jnl. Sound & Vibration*, 142(l), 1990

[6] Bremner P.G. & Wilby, J.F, "Aero-Vibro-Acoustics: Problem Statement and Model-based Design Methods," AIAA 2002-2551, *Proc. AIAA Aeroacoustics Conf.*, Breckenridge CO , 2002

[7] M. Hartmann, J. Ocker, T. Lemke, A. Mutzke, V. Schwarz, H. Tokuno, R. Toppinga, P. Unterlechner, and G. Wickern. "Wind noise caused by the A-pillar and the side mirror flow". *Proc. AIAA Aeroacoustics Conf.*, Colorado Springs, 2012.

[8] Careni, M., Aybay O. and Holst S. "Tandem Cylinder and Idealized Side Mirror Far-Field Noise Predictions Using DES and an Efficient Implementation of FW-H Equation ", AIAA-2011-2843, 2011

[9] Bremner P.G. "Vibro-acoustic Sources Under Aero-acoustic Loads" *Proc. AIAA Aeroacoustics Conf. Colorado Springs,* June 2012

[10] Bremner, P., Shaw, T. and Mendonca, F. "Introduction to Aero-vibro-acoustics with STAR-CCM+" *Proc. STAR Global Conf.*, Orlando, March 2013

[11] Lighthill, M.J. "On Sound Generated Aerodynamically. II. Turbulence as a Source of Sound," *Proc. R. Soc. Lond*. A 222 (1954)

[12] Picard, C., "Etat des lieux des techniques d'imagerie acoustique a la DRIA de PSA et perspectives, in S´eminaire GdR Acoustique des Transports, *Localisation de sources acoustiques sur les v´ehicules. Nouveaux developpements, INRETS*, Bron, May 2008

[13] Curle, N. "The Influence of Solid Boundaries upon Aerodynamic Sound" *Proc. R. Soc. Lond.* A 231 No. 1187, 1955

[14] Arguillat, B. "Etude experimentale et numerique de champs de pression parietale dans l'espace des nombres d'onde, avec application aux vitrages automobiles" *Ph.D. Thesis No 2006-14, Ecole Centrale de Lyon*, 2006

[15] C. Gabriel, S. Müller, F. Ullrich, R. Lerch. Measurement of the spatial coherence of surface pressure in the wake of a car's side mirror" *Proc. AIAA Aeroacoustics Conf. Berlin*, 2013

[16] Todter, C. and Bremner, P. "Direct Data to Memory Sensor Array" *US Patent Application No. PCT/US2013/073403*, Filing Date 05 December 2013.